Chem Catalysis

CellPress

Article

Magnetic fields enhance mass transport during electrocatalytic reduction of CO_2

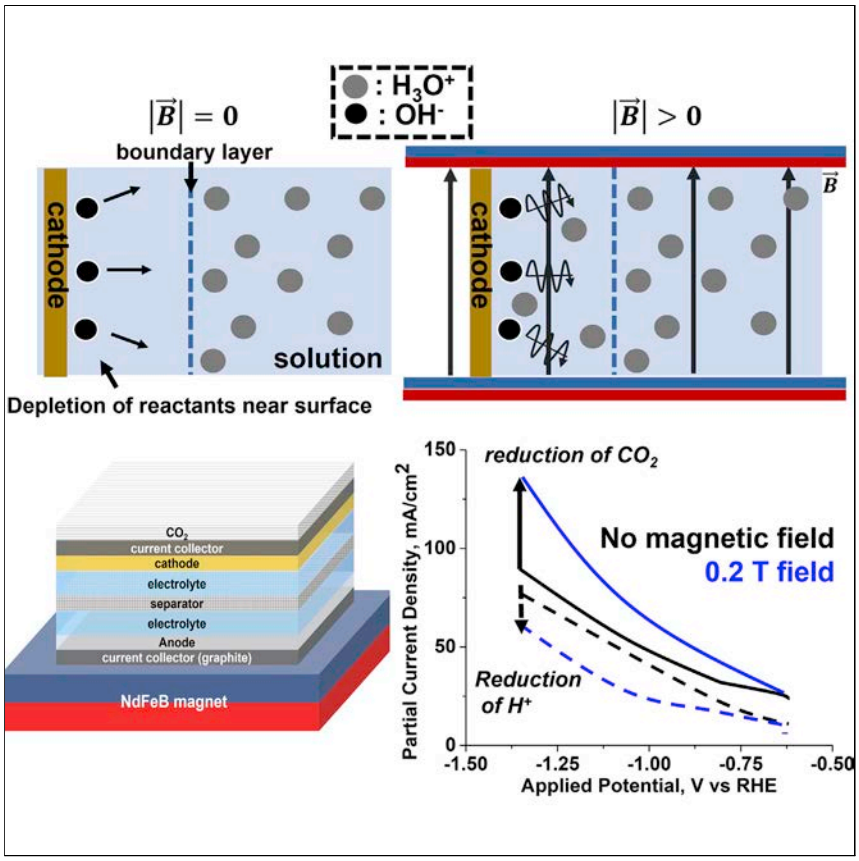

Magnetic fields parallel to the surface of an electrode can be used to increase mass transport during electrocatalytic reduction of CO_2.

Mohamad S. Kodaimati, Rui Gao, Samuel E. Root, George M. Whitesides

gwhitesides@gmwgroup.harvard.edu

Highlights

During CDR, magnetic fields (B-fields) generate convective currents in the fluid

The convection generated by B-fields decreases pH gradients during electrolysis

The magnitude of the B-field effect is dictated by the structure of the cathode

B-fields decrease the cost of operating a CO_2 electrolyzer by ~10%

Kodaimati et al., Chem Catalysis *2*, 797–815
April 21, 2022 © 2022 Published by Elsevier Inc.
https://doi.org/10.1016/j.checat.2022.01.023

Chem Catalysis

CellPress

Article

Magnetic fields enhance mass transport during electrocatalytic reduction of CO_2

Mohamad S. Kodaimati,[1,2] Rui Gao,[1,2] Samuel E. Root,[1] and George M. Whitesides[1,3,*]

SUMMARY

The selectivity of electrocatalytic reduction of CO_2 (CDR) is dictated not only by the intrinsic reactivity of the catalyst but also by the transport of reactants to the catalyst (i.e., mass transport). Current methods for increasing mass transport in CDR rely upon either (1) mechanical agitation or (2) use of gas-diffusion electrodes and are unable to eliminate concentration polarization completely. This work demonstrates that magnetic fields orthogonal to the ionic current (i.e., the Lorentz force) can be used to increase mass transport during CDR by generating convective flow in the fluid, thus modifying the observed selectivity of CDR. This increase in mass transport leads to a corresponding increase in current densities (up to 1.3× higher than the analogous system with no $\vec{B}$-field or agitation) and increased selectivity of CDR relative to the hydrogen evolution reaction (up to 2.5× higher than the system with no $\vec{B}$-field or agitation).

INTRODUCTION

Electrocatalytic reduction of carbon dioxide (CO_2; CDR) to products such as ethylene and methane[1–3] is a method for both (1) sequestering CO_2 and (2) producing chemical fuels compatible with carbon-based technologies.[4–11] Industrial implementations of CDR would require systems operating at high current densities (>100 mA/cm^2)[12,13] and with high Faradaic efficiencies (FEs) of ~100%. We define FE as: moles of product × number of electrons involved in the reaction / moles of electrons originating from the electrode.[14] In this chemical process, the hydrogen evolution reaction (HER) is competitive to CDR.[15]

Previous electrocatalytic methods for achieving high FEs and high current densities in CDR have relied upon careful selection of the electrode/catalyst materials,[16–19] the electrolyte,[11,20] and the electrochemical cell.[21,22] The hydrodynamics are important in electrochemical reactions such as CDR, which is limited by mass transport and generates concentration polarization. The Faradaic processes of CDR induce gradients in the concentration of protons/hydroxide ions and of CO_2 near the electrode surface; these gradients modify the relative rates for CDR and HER.[11] These gradients arise because: (1) bicarbonate is a weak buffer (and here allows for pH gradients)[23,24] and (2) the un-catalyzed exchange between CO_2 and carbonate/bicarbonate is slow. These rate constants represent spontaneous conversion of: 1) CO_2 and water to carbonic acid ($k_{carbonic\ acid} = 0.03\ s^{-1}$) and 2) CO_2 and hydroxide ions to bicarbonate ($k_{bicarbonate} = 2.2 \times 10^3\ M^{-1}/s$)[25,26] (Figure 1A). Concentration polarization of protons/CO_2 during CDR decreases the FE of CDR relative to HER (Figure 1B).[11,27]

Typical approaches for mitigating the undesirable effects of concentration polarization involve either: (1) increasing the rate of transfer of CO_2 to the electrode surface through a gas diffusion electrode (GDE) or (2) agitation of the solution (e.g., through

The bigger picture

At high current densities (>100 mA/cm^2), the electrocatalytic reduction of CO_2 (CDR) can be limited by mass transport, resulting in decreased selectivity for CDR relative to the reduction of protons to hydrogen. Common approaches to increase mass transport for CDR rely upon either (1) gas-diffusion electrodes or (2) mechanical agitation. This work demonstrates that magnetic fields acting through the Lorentz force can increase mass transport during CDR. Magnetic fields generate convective currents by the Lorentz force acting on ions moving during electrolysis and decreases the cost of operating a CO_2 electrolyzer (by ~10% in this work).

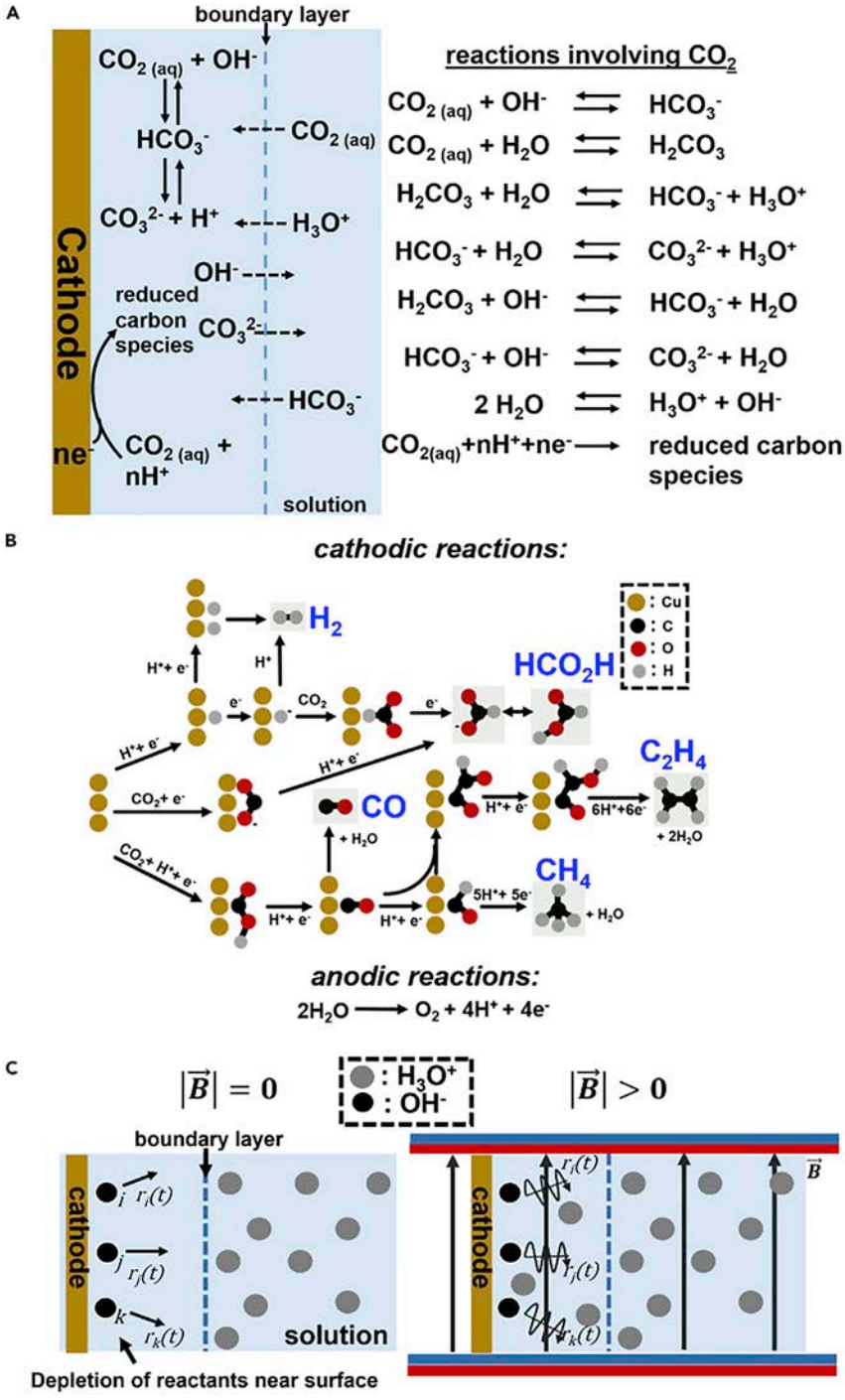

Figure 1. Schematic representation of the role of magnetic fields on the electrocatalytic reduction of CO_2 (CDR)

This work examines how selectivity of the cathodic reactions of CDR on a copper electrode is influenced by magnetic fields.

(A) Schematic representation of CDR and the mechanisms of concentration polarization near the cathode during CDR. Slow exchange between aqueous CO_2 and bicarbonate limits reactivity.

(B) Schematic representation of some of the reactions occurring in this system.[1] We observed two major sets of CDR reactions and HERs. Competition between these reactions and the products

[1]Department of Chemistry and Chemical Biology, Harvard University, 12 Oxford Street, Cambridge, MA 02138, USA

[2]These authors contributed equally

[3]Lead contact

*Correspondence: gwhitesides@gmwgroup.harvard.edu

https://doi.org/10.1016/j.checat.2022.01.023

Figure 1. *Continued*
formed is dependent upon both the intrinsic kinetics of the process and the concentration of species near the electrode surface.
(C) Schematic representation demonstrating the findings of this work. At high current densities, *j*, we observed depletion of protons near the electrode surface without a magnetic field (by Raman spectroscopy and by adding a pH indicator). In the presence of a magnetic field and at a high *j*, the concentration gradient near the electrode surface is less than in the case without a magnetic field. The black circles correspond to negatively charged species (i.e., hydroxide ions) formed at the cathode during CDR with black arrows ($r_i(t)$) corresponding to the position of species *i* at time t.

the bubbling of gas or pump-driven circulation). These approaches (even when used in combination), however, are not sufficient to eliminate concentration polarization at high current densities (>100 mA/cm^2).[28–33]

Although the influence of magnetic fields on electrochemistry has been studied for more than 60 years,[34–43] practical applications of magnetic fields in electrochemistry have been primarily limited to microfluidic devices.[39] Previous examples of using magnetism in electrochemistry have focused primarily on four effects: (1) magneto-hydrodynamics (MHD; using magnetic fields to generate convective currents),[38] (2) chirality-induced spin selectivity (using magnetic electrodes to inject electrons with relatively well-defined spin),[40] (3) magnetophoresis (using magnetic fields to control the motion of paramagnetic species with respect to the magnet),[41] and (4) stabilization of radical pairs[42,43] (using magnetic fields to stabilize radical pair spin states). For example, Pan et al.[42] recently reported that magnetic fields can increase yield of formate from CO_2 and attributed this effect to the magnetic field "enhancing the amount of single radical pairs via magnetic field-facilitated triplet—singlet spin evolution."[42] In this work, we propose a method complementary to mechanical agitation and GDEs for increasing mass transport and thus improving selectivity in CDR by exploiting the fluidic convection generated by magnetic fields (MHD),[44] mediated by the Lorentz force acting on ions. Although the Lorentz force has recently been used to increase mass transport on the anodic processes of CDR for a NiFe-based bimetallic catalyst,[45] in this work we demonstrate how the Lorentz force acts upon the cathodic processes of CDR to increase mass transport. The concentration of chemical species near the electrode dictates the observed rates for competing reaction pathways (Figure 1).

RESULTS AND DISCUSSION

This paper focuses on MHD effects and demonstrates that magnetic fields can be used to decrease spatial gradients of concentrations of reactants in electrocatalytic systems—and thus modify the observed selectivity (Figures 1B and 1C). We demonstrate the use of magnetic fields for modifying CDR; specifically, we examine the effects of interactions of a magnetic field with moving ions (i.e., electric current) generated by the electrocatalysis (i.e., the Lorentz force acting on ions). Ionic currents are generated in CDR because of (1) the production of protons at the anode and consumption of protons and carbonate/bicarbonate at the cathode and (2) the electrophoretic transport of products away from the electrode surface and reactants toward the electrode surface (Figure 1). When a static magnetic field, $\vec{B}$ [T], with components perpendicular to the ionic current is applied, the instantaneous force, $\vec{F}(t)$ [N], felt by an ion with charge, q [C], moving with instantaneous velocity, $\vec{v}(t)$ [m/s], can be expressed using the generalized Langevin form of the Lorentz force, following Equation 1,[46,47]

$$\vec{F}(t) = q\left(\vec{E} + \vec{v}(t) \times \vec{B}\right) - \int_0^t \gamma(t-t')\vec{v}(t')dt' + \vec{\xi}(t), \qquad \text{(Equation 1)}$$

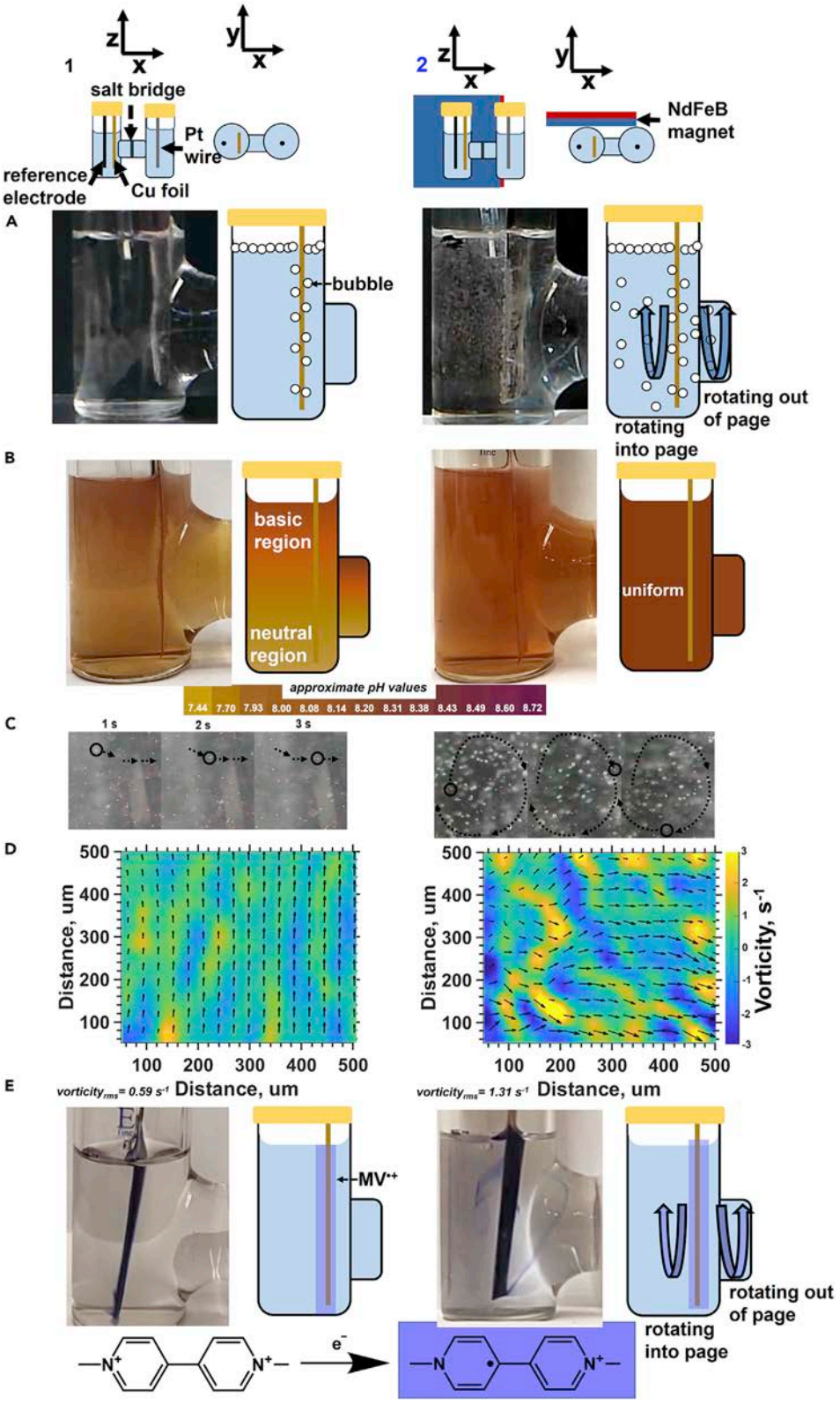
1
z
x
y
x
salt bridge
Pt wire
reference electrode
Cu foil
2
z
x
y
x
NdFeB magnet
A
bubble
rotating out of page
rotating into page
B
basic region
neutral region
uniform
approximate pH values
7.44 7.70 7.93 8.00 8.08 8.14 8.20 8.31 8.38 8.43 8.49 8.60 8.72
C
1 s
2 s
3 s
D
Distance, um
500
400
300
200
100
100 200 300 400 500
Distance, um
Vorticity, s-1
3
2
1
0
-1
-2
-3
E
vorticity_rms= 0.59 s-1
Distance, um
vorticity_rms= 1.31 s-1
Distance, um
MV•+
rotating out of page
rotating into page
e-
N+
N+
N
N+

Figure 2. Visual evidence of convective currents

We qualitatively compared mass transport in an electrochemical H cell in two configurations. The first configuration (i.e., the control experiment with B = 0) consisted of a Cu foil cathode, Ag/AgCl reference electrode, and Pt wire anode in an aqueous solution of 1.0 M $KHCO_3$ + 0.1 M KCl, at a potential of 1.1 V versus RHE. In the second configuration a four in x four in x one in NdFeB magnet was placed perpendicular to the Cu foil surface. The y component of the B-field near the Cu foil is ~0.3 T.

(A) Upon application of a magnetic field, we observed the generation of helical currents in the bubbles.

(B) After adding 0.5 mM metacresol purple (as a pH indicator), we observed the magnetic field decreases the pH gradient formed in the H cell upon electrolysis.

(C) After adding 5 μm red-colored polystyrene microspheres to the solution, we observed mixing in the bulk of the electrochemical solution under UV illumination. The arrows correspond to the trajectories of the particles.

(D) Particle-image velocimetry maps near the Cu foil surface of 3-μm fluorescent microspheres with and without an applied B-field. Arrows indicate velocity vectors, and colors indicate the derived vorticity. The root-mean-square (RMS) vorticities for samples with no applied field and an applied field were 0.59 and 1.31 s^{-1}, respectively.

(E) Schematics and pictures of the colorimetric reaction we explored to understand how magnetic fields interact with electrochemistry/electrocatalysis. We explored the reversible one-electron reduction of methyl viologen (MV^{2+}) to form methyl viologen radical ($MV^{\bullet+}$). $MV^{\bullet+}$ has a deep blue color. After adding MV^{2+}, we observed similar helical currents being formed upon application of the magnetic field. The dark color near the Cu foil is $MV^{\bullet+}$. Horizontal lines in pictures correspond to the bottom edge of the H cell.

where $\int_0^t \vec{\gamma}(t-t')\vec{v}(t')dt'$ represents the drag on the ion and is obtained from a memory kernel integral of the dynamic (i.e., frequency-dependent) friction coefficient, $\gamma(t)$. The term $\vec{\xi}(t)$ is a stochastic force representing noise induced by collisions with solvent molecules. Equation 1 predicts that a charged particle in solution experiences a force in the direction of $\vec{E}$, a force orthogonal to the velocity of the particle and to $\vec{B}$ (following the right-hand rule), and field-independent drag and stochastic forces resulting from collisions with solvent molecules. These frictional interactions mediate the translation of the Lorentz force acting on the ions into hydrodynamic flow within the fluid at the electrode surface.

Particularly in the case of a planar electrode (Figure 1C), charged species approaching the surface of the electrode have a velocity component perpendicular to the surface of the electrode.[37] This ionic "current" can interact with an orthogonal magnetic field (i.e., in the plane of the surface of the electrode) to induce helical motion in these ions—generating convection within the fluid that enhances the mass transport and, thus, the mass transport-limited current.[38] For single-step electrochemical reactions, the effect of the magnetic field may be limited to enhancing the observed current; however, for multi-step reactions, such as CDR, we would expect to observe changes in reactivity/selectivity as well (because the rate equations are non-linear).

To explore the effect of a magnetic field ($\vec{B}$-field) on CDR, we performed electrolysis with a polycrystalline Cu foil cathode and a Pt wire anode in an electrochemical H cell: (1) with no $\vec{B}$-field and (2) with a $\vec{B}$-field oriented perpendicular to the Cu foil (Figure 2). We applied a $\vec{B}$-field by placing a 4 × 4×1-inch neodymium iron boron (NdFeB) magnet perpendicular to the surface of the Cu foil (shown in Figure 2). We used the following xyz coordinate space to describe the reference frame of our experiments: the x coordinate is perpendicular, and the y and z coordinates are parallel to the plane of the Cu foil. The y component of the $\vec{B}$-field is ~0.3 T at the surface of the Cu foil (with the x and z components ~0 T). We used aqueous solutions of 1.0 M $KHCO_3$ (which served three functions: [1] a buffer, [2] a source of CO_2, and [3] as a supporting electrolyte) + 0.1 M KCl (which also served as a component of the supporting electrolyte) and a Ag/AgCl reference electrode. CO_2 was bubbled through the solution to remove O_2 and N_2 (from dissolved air). At the anode, we observed only the oxygen evolution reaction (OER), whereas at the cathode, we observed both CDR and HER (Figure 1). We focus on the effects of a $\vec{B}$-field on the cathodic reactions unless otherwise noted.

Visual evidence of convective currents

During electrolysis, we observed that (1) with no $\vec{B}$-field, the bubbles rise to the top of the solution and (2) in the presence of an applied $\vec{B}$-field, the bubbles and the fluid undergo helical rotations in the solution parallel to the plane of the Cu foil (Figure 2A; Videos S1 and S2). The direction of rotation for the bubbles/fluid is consistent with electrophoresis of protons (positive charges) toward the cathode and/or electrophoresis of hydroxide ions (negative charges) away from the cathode, following the right-hand rule (Equation 1; Figure 1). In addition to transport of protons toward the cathode and hydroxide ions away from the cathode, we expect to observe transport of bicarbonate toward the cathode and transport of carbonate away from the cathode. The net ionic current involves positive ions moving toward the cathode (or negative ions away from the cathode), where the ionic current is equal in magnitude and opposite in sign to the electric current flowing between the cathode and anode. When we changed the orientation/direction of the $\vec{B}$-field by moving or flipping the NdFeB magnet, we observe rotations in the fluid consistent with the right-hand rule and the above-noted ionic currents (Figure S2). We would expect to see a weak Hall effect because of the Lorentz force acting upon electrons moving through the copper cathode.[48] We exclude the Hall effect because the voltage difference generated by the Hall effect ($\sim 10^{-7}$ V) is much smaller than the voltages applied to the electrochemical cell (~1–2 V).

To determine the effect of the fluid motion on the macroscopic pH gradients in the electrochemical cell, we added a pH indicator (0.5 mM metacresol purple in a solution of supporting electrolyte) (Figure 2B; Videos S3 and S4). Over the course of 5 min of electrolysis, we observed heterogeneity in the pH of the solution within the electrochemical cell, presumably because of the fact that the rate of consumption of protons at the cathode exceeds the rate of transport of protons from the anode to the cathode. When we ran the experiments at a lower potential (and thus lower current) but increased the electrolysis time to allow for the same amount of charge (integrated current) to pass through the system, we did not observe the formation of a pH gradient—supporting this hypothesis (Figure S3; Video S5). When we performed electrolysis with a $\vec{B}$-field, we observed that the helical currents of the solution induced rapid mixing and a uniform pH within the solution (Figure 2B).

By adding 5-μm-diameter red polystyrene microspheres to the solution, we observed the solution was mixed upon application of a $\vec{B}$-field by analyzing the trajectories of the microspheres, supporting our hypothesis of $\vec{B}$-fields enhancing mass transport for CDR (Figure 2C; Videos S6 and S7). To determine whether the $\vec{B}$-field was generating convection near the surface of the Cu foil, we analyzed the fluid flow near the electrode surface using particle-imaging velocimetry (PIV) with 3-μm-diameter fluorescent polystyrene microspheres.[49] We observed that the presence of a magnetic field increased the turbulence and mixing of the solution near the electrode as evidenced by the fluid's velocity field and vorticity, which is defined as the curl of the velocity field[48] (Figure 2D). See the supplemental information for details (Figure S4). We suspected that the convective mixing in the solution was generated by protons/hydroxide ions in solution because most of our observed products for CDR were neutral and near-zero magnetic susceptibilities (e.g., H_2, CO, and CH_4). These helical flows are not unique to CDR; we have observed similar results in the single-step electrochemical reduction of methyl viologen (MV^{2+}) to the radical species ($MV^{\bullet+}$) using the same electrochemical cell (Figure 2E; Videos S8 and S9). In this case, MV^{2+} is colorless, whereas $MV^{\bullet+}$ is identified by its blue color and reverts to MV^{2+} upon exposure to oxygen.[50] In the case of the reduction of MV, a net

positive current flows toward the cathode (which results from transport of MV^{2+} toward the cathode and of $MV^{\bullet+}$ away from the cathode). We did not observe helical flows in the absence of a magnetic field (Figure S5). We performed control experiments with $MV^{2+}(PF_6^-)_2$ (in dimethyl sulfoxide [DMSO]), indicating this effect occurred independently of the chemical nature of this "ionic" current. See the supplemental information for details (Figure S6).

In all the above experiments, we observed a reversal in the direction of rotation when switching the direction of the magnetic field, consistent with the Lorentz force. We also observed that moving the orientation of the magnetic field relative to the ionic current (by moving the NdFeB magnet) modified the orientation of the helical flows following the right-hand rule (Equation 1). From our visual experiments, we drew the following conclusions: (1) helical/convective currents were generated by the Lorentz force acting on ions within the fluid, and (2) these convective currents enhanced mass transport/mixing in the bulk of the solution and near the surface of the electrode. These experiments are consistent with previous reports[34,38] that the Lorentz force acting on ions results in convective motion of the fluid because of the interaction of the moving ions on the fluid through the viscous drag force (Equation 1). This induced motion of the fluid is visualized by the movement of the bubbles and tracer particles.

Raman spectroscopy

To determine whether the Lorentz force enhanced mass transport near the electrode surface, we employed confocal Raman microscopy to measure the approximate pH near the electrode surface. The concentrations of bicarbonate, carbonate, and CO_2 have been shown to be out of equilibrium near the surface of the electrode,[23] and we measure the approximate pH to determine how electrolysis with and without a magnetic field shifts pH gradients formed near the electrode. We examined the Raman peak of bicarbonate at 1,019 cm^{-1} and Raman peak of carbonate at 1,070 cm^{-1} (Figure 3B).[28] We compared the ratio of the area of bicarbonate and carbonate peaks (after correcting for differences in their Raman cross-sections) to determine the approximate pH near the electrode surface.[28] We determined the pH of the solution from the relative areas of the bicarbonate/carbonate Raman peaks following Equation 2:

$$\mathrm{pH} \approx -\log\left(\frac{\mathrm{area}_{\mathrm{bicarbonate}}}{\mathrm{area}_{\mathrm{carbonate}}} \times C\right) + \mathrm{pkA}_{\mathrm{bicarbonate}} \qquad \text{(Equation 2)}$$

where C is a constant (obtained from a calibration curve) (see the supplemental information for details). By moving the focal point of the microscope relative to the sample, we measured the pH at three distances from the Cu foil surface: 5 $\pm$ 4 μm (Figure 3C), 500 $\pm$ 4 μm (Figure S9), and 1,000 $\pm$ 4 μm (Figure 3D) throughout electrolysis (−0.8 V versus reversible hydrogen electrode [RHE]). At 5 $\pm$ 4 μm from the Cu, we observed a rapid increase in the solution pH from ~7.8 to ~8.6 within 30 s of applying the cathodic potential, which is consistent with consumption of protons at the cathode. Notably, we observed that the presence of the $\vec{B}$-field decreases the pH of the solution from 90 s until 720 s (the end of the experiment). At large distances from the electrode surface (500 and 1,000 μm) in the absence of a magnetic field, the pH of the solution remained largely unchanged during the duration of the experiments, which is consistent with our visual experiments and primarily diffusion-driven transport. Upon application of the 0.3-T $\vec{B}$-field, we observed an increase in the pH when the focal point was 500 and 1,000 μm away from the electrode surface, which was consistent with our visual experiments of convective transport generated by the magnetic fields. The combination of decreasing the pH near the electrode and

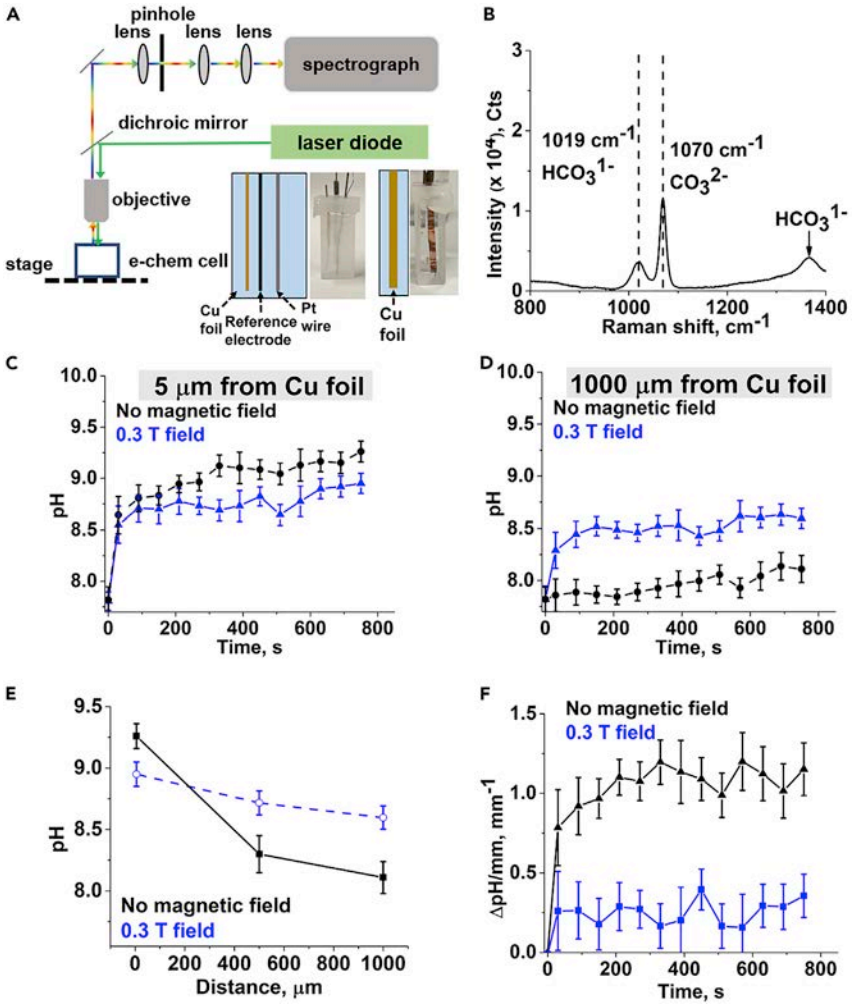

Figure 3. Raman spectroscopy during electrolysis

(A) Pictures and schematic of the electrochemical cell we used for *in situ* Raman measurements. The electrochemical cell consists of a glass cuvette with copper foil cathode, Ag/AgCl reference electrode, and Pt wire anode submerged in 1 M $KHCO_3$. We used this electrochemical cell in conjunction with a Horiba LabRam confocal Raman microscope to collect *in situ* Raman spectra.

(B) Representative Raman spectrum showing peaks corresponding to bicarbonate and carbonate at 1,019 and 1,070 cm^{-1}, respectively.

(C and D) Plots showing pH of solution at distances of 5 μm (C) and 1,000 μm (D) from the Cu foil surface as a function of electrolysis time.

(E) pH as a function of a distance after 750 s of electrolysis under no field (solid, black) and with 0.3-T field (dashed, blue).

(F) From these plots, we extracted the change in pH (ΔpH) per millimeter via a linear fit (F). Samples with 532 nm excitation (10 mW) and collected on a cooled charge-coupled device (CCD) with 200-μm pinhole and 600 gr/mm grating with an applied potential of −0.8 V versus RHE. Error bars represent the error propagated from a single experiment using the fitting procedure outlined in the supplemental information.

increasing the pH farther away from the electrode resulted in a decrease in the effective pH gradient near the electrode surface (Figures 3E and 3F). From the Raman microscopy and visual experiments, we concluded that the magnetic field enhanced convective mixing within the bulk of the solution and near the surface of the electrode. These results are consistent with previous reports of MHD effects in electrochemistry.[23]

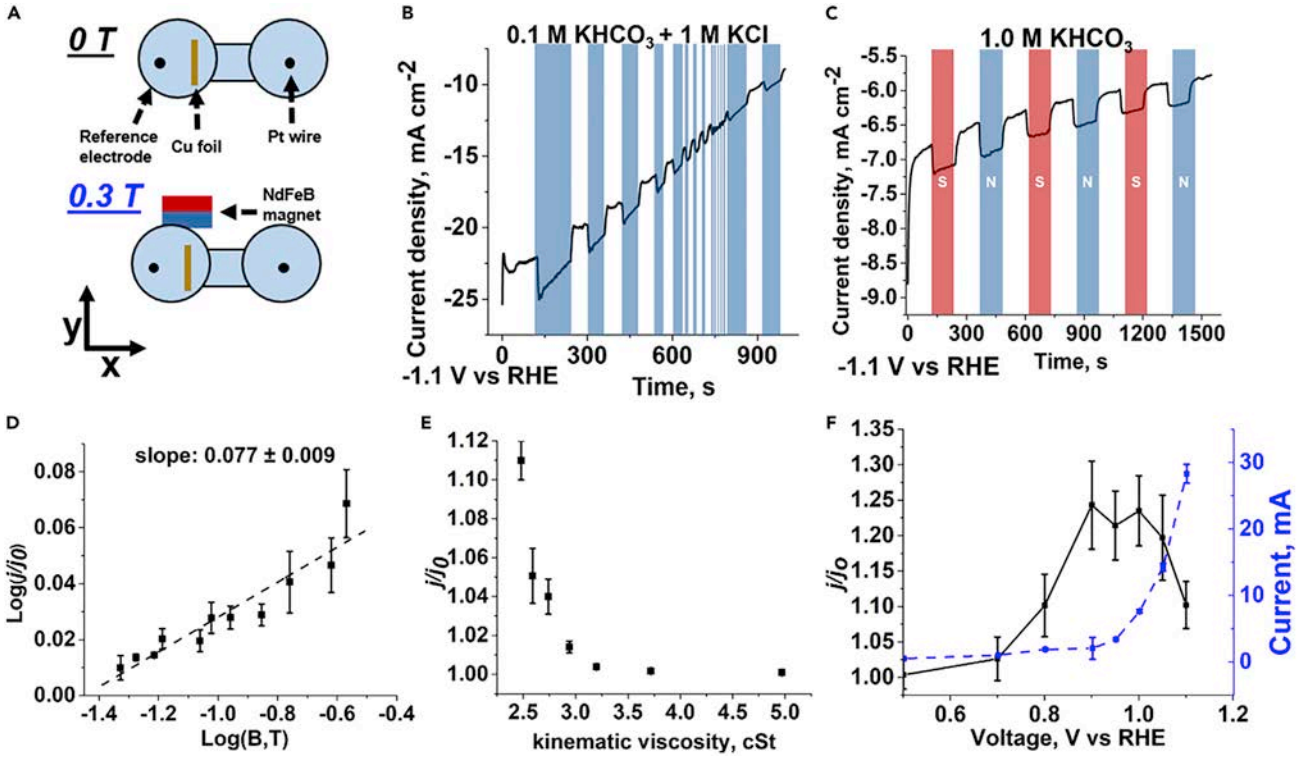

Figure 4. Electrochemical evidence of magnetic field effects

Enhancement of current density in CDR upon application of a magnetic field.

(A) Schematic diagrams of the electrochemical H cell used. We compared data with and without a magnetic field by placing a 2.5 × 2.5 × 5 cm NdFeB magnet perpendicular to the surface of the Cu foil.

(B) Amperometry measurements at a potential of −1.1 V versus RHE with 0.1 M $KHCO_3$ + 1 M KCl electrolyte. Blue regions correspond to time periods with the north face of the NdFeB magnet being placed perpendicular to the surface of the Cu foil (~0.3-T B-field).

(C) Amperometry measurement of our cell at a potential of −1.1 V versus RHE with 1 M $KHCO_3$. Blue (red) regions correspond to time periods with the north (south) face of the NdFeB magnet being placed perpendicular to the surface of the Cu foil (~0.3-T B-field).

(D) Plot of $\log(j/j_0)$ versus log(B) for samples collected using 0.1 M $KHCO_3$ + 1 M KCl aqueous solutions with the B-field parallel to the Cu foil (black) or B-field perpendicular to Cu foil (blue). Field strength was changed by modifying the distance between the Cu and the magnet. The dashed lines are linear fits to the data.

(E) Plot of j/j_0 versus kinematic viscosity for samples collected using solutions composed of 0.1 M $KHCO_3$ + 0.5 g/9 mL PEG with the y component of the B-field ~0.3 T (x,z ≈ 0 T). Error bars at viscosities greater than 3 cSt are too small to see.

(F) Plot of j/j_0 versus voltage current density. The current density was modified by changing the potential applied to the cathode. The error bars were calculated as the SD from n = 7 experiments.

Electrochemical evidence of convective currents

To quantify the effect of the Lorentz force on the transport-limited current density for CDR, we performed amperometry while placing (and subsequently removing) a permanent magnet perpendicular to the Cu foil surface (Figure 3A). We observed an increase in the current density upon applying a $\vec{B}$-field, and this enhancement was built within ~10 s of applying the $\vec{B}$-field. Similarly, this enhancement decayed within ~10 s of removing the $\vec{B}$-field. In the case of changing the magnitude of the $\vec{B}$-field (by removing and replacing the magnet) in a time less than 5 s, we observed no changes in current density, but, rather, a time average of the values observed with and without a $\vec{B}$-field. These observations are consistent with the enhancement in current density being due to increasing mass transport of protons and CO_2 (Figure 4B). Since the time scales for switching of the magnetic field by moving the magnet (~1 s) are much slower than the time scales for individual reactions in CDR, we believe the selectivity and current density will be dictated by the duty ratio rather than the switching frequency. We did not observe any differences

by flipping the poles of the magnet—and the direction of the $\vec{B}$-field (Figure 4C). We observed this effect only of the $\vec{B}$-field on the cathode and did not observe this effect of the $\vec{B}$-field on the Pt wire anode because O_2 evolution is generally electron transfer limited (Figure S10A).[51] When we applied a 0.3-T $\vec{B}$-field to a planar Pt mesh anode, we also did not observe any changes in the current density (Figure S12). When we increased convection in the cathodic compartment of the H cell via stirring (using either a magnetic stirring bar or electric motor), we observed an increase in the current density (Figure S13). When we increased convection in the anodic compartment of the H cell, we observed no change in the current density (Figure S10B). This observation is also consistent with CDR being mass transport limited[11] and OER being electron transfer limited.[51]

We observed an increase in the limiting-current density across different electrode materials and electrochemical cell geometries. The independence of the material and geometry of the electrode indicate that this enhancement in current density is related to the cathodic reactions, rather than the composition and shape of the cathode (Figure S14). We excluded magnetic field effects involving interactions with paramagnetic species, namely, effects of gradients in concentration of paramagnetic species and the field-gradient force, by performing experiments where we changed the gradient of the $\vec{B}$-field while maintaining the same magnitude and direction of the $\vec{B}$-field (Figure S22). Interactions of species with high magnetic susceptibilities (such as paramagnetic species) depend on the strength of the magnetic field, as well as the gradient of the magnetic field.[36] When we increased the uniformity of the magnetic field by placing the H cell in the center of two NdFeB magnets, we did not observe any changes to the $\vec{B}$-field effects. Similarly, we ruled out magnetic field effects on radical-pair states for the following reasons: (1) the onset potential and shape of linear-sweep voltammograms did not change upon applying a magnetic field (Figures S20 and S21); and (2) when we applied a uniform magnetic field orthogonal to the surface of the Cu foil (i.e., parallel to movement of ions in the system) (Figure S23), we observed no magnetic field effects. The interaction of magnetic fields with radical-pair states does not depend upon the macroscopic orientation of the magnetic field, ruling out interactions with radical-pair states as the dominant mechanism. In Figures S20 and S21, we observed no changes in the onset potential for CDR upon application of a magnetic field. Radical-pair spin-state effects should manifest as a change in the onset potential because they modify the overpotential associated with CDR. Radical-pair spin-state effects also do not depend on the orientation of the magnetic field; radical-pair spin-state effects depend only on the magnitude of the magnetic field. We observed that the magnetic field needs to be parallel with the cathode surface (orthogonal to the ionic current) to observe a change in CDR (Figures S22 and S23).

To quantify the magnitude of the enhancement, we introduced the term j/j_o (j and j_o refer to the current density in the presence and absence of a $\vec{B}$-field, respectively). Previous experimental and theoretical works have shown that a $\vec{B}$-field parallel to a planar electrode can increase the mass-transport-limited current for electrochemical reactions;[37,52,53] the Lorentz force increases the hydrodynamic flow near the electrode-solvent interface through convection and decreases the thickness of the diffusion layer. Lioubashevski et al.[37] derived a scaling relationship between the limiting current, I_l [A] and $\vec{B}$-field strength in the case of a homogeneous magnetic field parallel to the surface of a planar semi-infinite electrode:

$$I_l \propto A^{\frac{5}{6}} \rho^{-\frac{1}{3}} D^{\frac{8}{9}} \nu^{-\frac{2}{9}} C^{\frac{4}{3}} B^{\frac{1}{3}} \qquad \text{(Equation 3)}$$

where A (m^2) is the area of the electrode, ρ (kg/m^3) is the specific density of the fluid, D (m^2/s) is the diffusion constant of the electrolyte, ν (m^2/s) is the kinematic viscosity, C (M) is the concentration of the electroactive species, and B (T) is the magnitude of the magnetic flux density.[37] Lioubashevski et al.[37] assume the reactants/products are diamagnetic and soluble within the solution, and as such, one discrepancy between Lioubashevski et al.'s assumptions and our experiments is the formation of bubbles in CDR.

Generally, we observed qualitative and quantitative discrepancies between those predicted by Equation 3. When we varied the magnetic field strength by changing the distance between the permanent magnet and the electrode, we observed that j/j_o scales with $B^{0.08}$ (Lioubashevski et al.[37] estimated $B^{1/3}$)—in less strong agreement with Equation 3 and Figure 4D. We believe the weak dependence of the current density on the B-field ($\propto B^{0.08}$) arises because of a convolution of (1) the effects of the B-field on mass transport, (2) the effects of bubble evolution on mass transport, and (3) the effects of the B-fields on the product selectivity (Figure S27) and effects of product selectivity on bubble evolution (buoyance of gas products formed).

To further test the relationship between j/j_0 and the $\vec{B}$-field, we changed the viscosity of solutions (while maintaining a constant dielectric constant) from 2.48 to 4.97 cSt by comparing solutions with fixed concentrations (0.0556 g/mL) of polyethylene glycol (PEG) and differing molecular weights (0.4–35 kg/mol). Although we observed a negative correlation between the kinematic viscosity and j/j_0, this relationship did not follow a simple power law (Figure 4E).

Furthermore, we found that increasing the surface area, current density, and viscosity of the solvent could produce a non-monotonic relationship with j/j_o. For example, Figure 4F illustrates how an increase in the current density—achieved by increasing the applied potential—led to a non-monotonic relationship between the current density and j/j_0. We suspect these differences arise because the primary cathodic products are gaseous (H_2, CO, CH_4, and C_2H_4). These products are subject to buoyancy and solubility, and the removal of bubbles (composed of these products) generates convection.[54] No previous reports of MHD effects in electrochemistry have demonstrated these non-monotonic relationships. When we examined a reaction that does not generate gaseous products (reduction of camphor-sulfonic acid to the corresponding alcohol), we observed empirical trends consistent with previous reports of MHD effects for electrochemical reactions (Figure S15), supporting our hypothesis that the convection generated by the bubbles produced this non-monotonicity.

Because commercial implementations of CDR require high current densities, and thus rough/micro-structured electrodes, we explored the relationship between the effect of a magnetic field on convective mixing and the electrochemical surface area (ECSA) of the cathode to determine the effectiveness of MHD in nanostructured electrodes (Figure 4). We used electrodes with the same physical dimensions/area but with differing morphologies/roughness to modify the ECSA of the cathode (see the supplemental information for details). We inferred the ECSA of the electrodes by measurements of capacitance (Figure S19).[14] In brief, we observed three distinct regimens relating the ECSA to j/j_0. Regimen I corresponded to a cathode (with a relatively smooth surface) with a low ECSA, where we observed a roughly linear relationship (similar to Equation 3). Cathodes in regimen I included mechanically polished Cu foil and Cu foil subjected to treatment with an O_2 plasma. Regimen II corresponded to Cu foams and consisted of a high ECSA cathode with microscopic

roughness (approximately hundreds of micrometers) with high current densities and j/j_0. Finally, regimen III consisted of CuO nanowires obtained by etching Cu foil[55] and corresponded to nanostructured electrodes with high ECSA and low j/j_0 (~1.01). We suspect the differences between the three regimens primarily arise because of changes in fluid flow caused by changes in the geometry of the surface (i.e., the Reynold's number). For example, the pores in the Cu foam are ~150 μm in diameter, while the pores in the Cu nanowires are <1 μm in diameter; these values result in different regimens of fluid flow. As such, we expected the fluid flow in the nanowires to be more laminar than in the foam, and thus impeding the convective mixing generated by the magnetic fields. By analyzing the fluid flow in each case using PIV, we observed higher vorticity in the case of the Cu foam and lower vorticity for the CuO nanowires, confirming the hypothesis that the nature of the fluid flow in each of these three regimens is different (Figures 1D, 4E, and 4F). Finally, we observed that the relative effectiveness of convection generated by mechanical agitation versus by the Lorentz force differed based upon the relative surface roughness of each electrode. In the case of the relatively smooth Cu foil electrodes, mechanical agitation was more effective and increased the current density by up to three times higher than the increase in current density achieved by application of $\vec{B}$-field. In the case of the CuO nanowires, the B-field increased the current density by as much as four times the increase in current density achieved with stirring, and for the Cu foam, the B-field increased the current density by as much as two times the increase in current density achieved with stirring. We observed that the roughness of the catalyst surface determines the effectiveness of the convective mixing generated by magnetic fields—previously not considered by chemists but well known by physicists.[44]

Modifying selectivity for CDR

To determine the effect of a magnetic field on the selectivity of the CDR, we analyzed the distributions of products obtained using Cu foam for the cathode (after 15 min of electrolysis). We did not examine shorter time spans. We compared the products in three systems: (1) CDR without a $\vec{B}$-field, (2) CDR with a $\vec{B}$-field, and (3) CDR with mechanical agitation (stirred with a paddle attached to a direct current (DC) motor spinning at 6,000 rpm) (see the supplemental information for details). Concentrations of gases formed during the reaction were measured by gas chromatography (GC), and liquids formed in the aqueous phase were measured using ^{1}H-NMR using an internal standard (DMSO) (see the supplemental information for details). The values reported correspond to the average value from three independent experiments. We observed that the application of a magnetic field increased the proportion of CDR products to hydrogen gas across all potentials measured (0.7–1.1 V versus RHE), but the difference between no convection (the experiments carried out with no $\vec{B}$-field) and convection (via stirring the electrochemical cell with a DC motor or applying a $\vec{B}$-field) in CDR versus HER selectivity increases at higher potentials, which is consistent with increased concentration polarization at higher current densities decreasing the selectivity of CDR relative to HER (Figure S27). Notably, we observed that the magnetic fields increased CDR selectivity relative to hydrogen gas production (up to 2.5 times higher than the system with no convection at 0.95 V versus RHE and 1.5 times higher than a model system mechanically mixed with a motor at 1.1 V versus RHE). We observed that these trends are *not* unique to this cathode; when we used either a gold film cathode or polycrystalline copper foil cathode, we also observed increased CDR versus HER selectivity (Figures S25 and S26). Our observed results are consistent with previous reports that increasing mass transport increases the selectivity of CDR versus HER.[11,27] A preliminary energetic analysis indicates that the convection generated by the DC motor consumed ~30 mW of

electricity during operation, whereas electrolysis consumed ~20–30 mW of electricity. Recent analyses of the potential operating costs associated with industrial-scale CDR estimate the electricity consumed while operating an electrolyzer to be ≥20% of the total operating costs.[3,15,56] Specifically, a Lorentz force-based approach to mixing uses the potential energy stored within concentration gradients formed at the electrode surface to mix the fluid *near* the surface decreases the energy consumption of the entire system and increases the selectivity for CDR products, whereas mechanical mixing-based approaches *expend additional energy* to mix the solution. Finally, we also observed that Lorentz force-based mixing is compatible with mechanical agitation methods; namely, the Lorentz force enhances mixing and the current when used in combination with a peristaltic pump (see Figure S26).

Effect of magnetic fields on flow cells with GDEs

To examine the effectiveness of using magnetic fields to increase mass transport at high current densities (~100 mA/cm^2), we measured the effects of a 0.2-T field on CDR in a flow cell with a GDE. In brief, we used 25-nm Cu nanoparticles spray-coated on one side of carbon paper as the cathode and a Pt mesh as the anode with graphite serving as the current collectors (Figure 6A). We flowed CO_2 through the uncoated side of the GDE while flowing 1 M $KHCO_3$ over the cathode and anode. The cathodic and anodic chambers were separated by a Nafion 117 membrane, and we used Ag/AgCl as a reference electrode in the cathodic chamber. In all cases, we flowed CO_2 at 30 sccm. The supplemental information contains additional details concerning the GDE experiments (Figure S28).

When we compared the current density at different flow rates for the catholyte averaged over 10 min of electrolysis, we observed that an increase in the flow rate from 7 to 60 mL/min did not appreciably change the current density between ~−1 and 0 V but increased the current density by up to ~17% (Figure 6B). These results are consistent with our correlation of the magnitude of the enhancement of the current with the roughness of the electrode; the GDE is microporous with pore sizes of ~100 μm (Figure S29), which corresponds to regimen II of Figure 5A. When we compared the current density with and without a magnetic field at a flow rate of 7 mL/min, we observed larger differences in the current density of ~28%. To disentangle the contributions of HER and CDR to the current density, we used GC and NMR to determine the partial current densities corresponding to HER and CDR (see the supplemental information for details). In this system, we observed that the majority of products were H_2, CO, CH_4, C_2H_4, and $HCOO^-$. When we compared the partial current densities for CDR with and without a magnetic field, we observed that we were able to increase the partial current density of CDR by ~50% at the same potential of 1.3 V versus RHE (Figure 6C). To achieve the same partial current density of ~85 mA/cm^2 for CDR, we decreased the cell potential (including the internal resistance of the cell) from 2.2 to 1.9 V. The increase in partial current density of CDR is due to the 17% increase in overall current density and a ~20% increase in the FE of CDR.

To evaluate the potential cost-effectiveness of using magnetic fields for CDR, we performed a preliminary techno-economic analysis adapted from Shin et al.[57] (see the supplemental information for details). In this analysis, we assume the following: (1) the primary product formed is ethylene, (2) the cost of electricity is \$0.03 kWh^{-1}, (3) the cell potential is decreased by ~10% from 5.9 V without a magnetic field to 5.3 V with a magnetic field, and (4) the cost of an NdFeB magnet is ~\$75/kg. From this analysis, we estimated that we could decrease the cost of production of

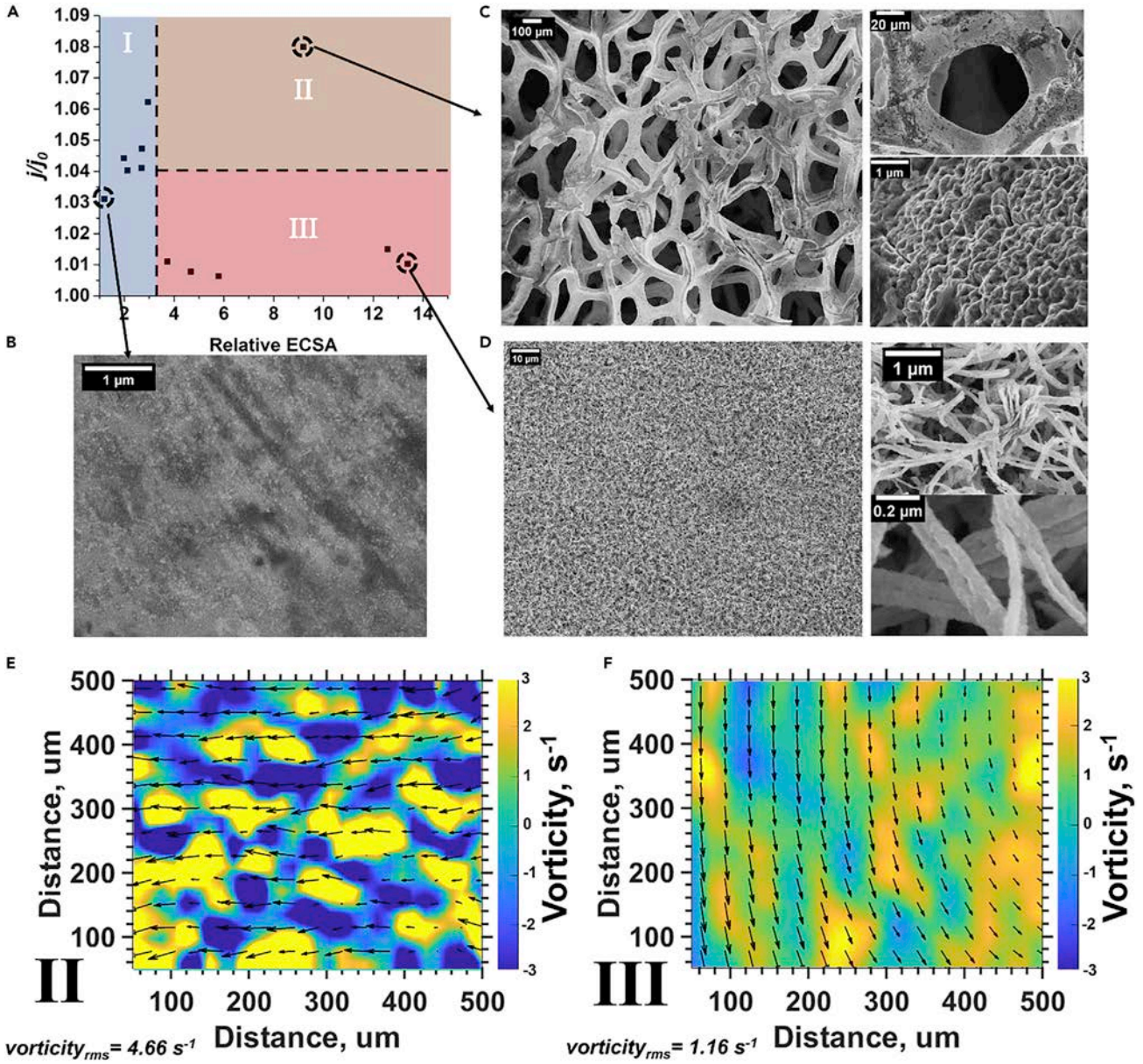

Figure 5. Relationship between electrochemical surface area and magnetic field effects

(A) Plot of j/j_0 versus relative ECSA for samples where we varied the structure of the cathode. We identify three regimens: I, low surface area electrodes (blue); II, macroscopically rough surfaces; and III, nanoscopic rough surfaces.

(B–F) Representative scanning electron microscopy (SEM) images of Cu foil (B), Cu foam (C), and CuO nanowires (D) corresponding to regimens I, II, and III, respectively. PIV maps near the surface Cu foam (E) and CuO (F) nanowires of 3-μm fluorescent microspheres with a 0.3-T B-field. Arrows indicate velocity vectors, and colors indicate the derived vorticity (curl of the velocity field). The RMS vorticities for the Cu foam and CuO nanowires are 1.16 and 4.66 s^{-1}, respectively. PIV maps correspond to the plane and were not collected at the same absolute position relative to the magnet. The different directions of the velocity fields are due to the macroscopic helicity (~2 cm) of the velocity fields.

ethylene from ~$3.40 to $3.09 kg^{-1} (Figure 6D). Although the NdFeB magnet increases the price of the electrolyzer from $4,300/$m^2$ to $5,800/$m^2$, this price increase is offset by the decrease in the power consumption of the system (here, we assume the magnetic field decreases the voltage required to operate the cell at a fixed current density). Although this analysis is preliminary, our analysis and previous analyses indicate that the electrical efficiency primarily dictates the cost to produce chemicals

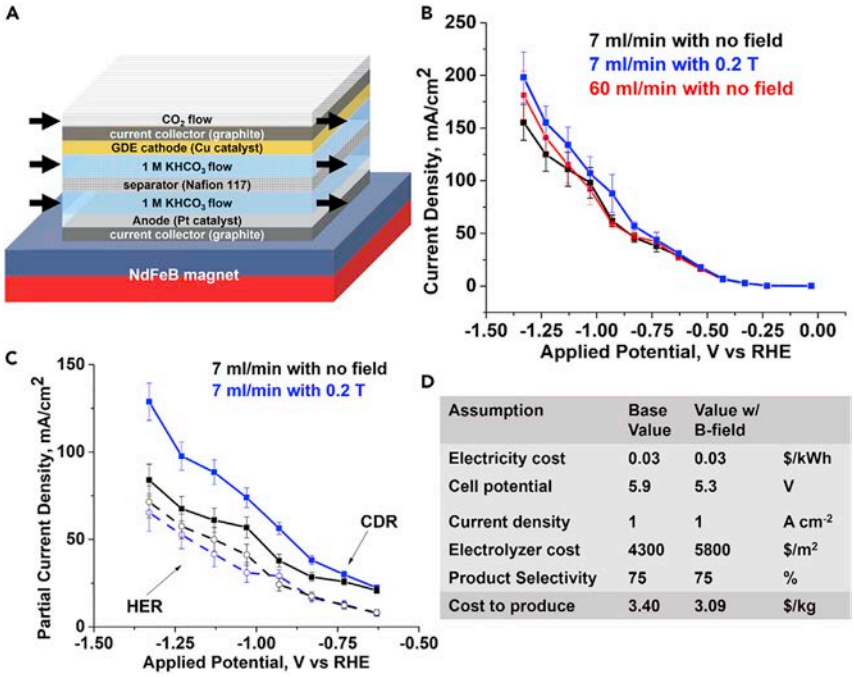

Assumption	Base Value	Value w/ B-field	
Electricity cost	0.03	0.03	$/kWh
Cell potential	5.9	5.3	V
Current density	1	1	A cm^{-2}
Electrolyzer cost	4300	5800	$/m^2
Product Selectivity	75	75	%
Cost to produce	3.40	3.09	$/kg

Figure 6. Effect of magnetic fields on a gas diffusion electrode

(A) Schematic representation of the GDE flow cell that we used in these experiments.

(B) Current density as a function of applied potential versus RHE without a magnetic field at 7 mL/min (black), with a 0.2 T field at 7 mL/min (blue), and without a magnetic field at 60 mL/min.

(C) Plots of partial current density versus applied potential for samples after 20 min of electrolysis for CDR products (solid) versus HER (dashed) products for the case of no magnetic field with the electrolyte flowing at 7 mL/min (black) and 0.2-T field flowing at 7 mL/min. Values represent the average of three independent experiments, and bars correspond to the 99% confidence intervals (CIs) of these experiments. The gas-phase products were quantified using GC, and formate was quantified using ^{1}H-NMR.

(D) Table of estimated cost savings of the magnetic field on CDR.

Details are in the supplemental information.

via CDR, rather than capital costs. As such, we believe magnetic fields may be one method for increasing the electrical efficiency and lowering the cost of CDR.

Conclusions

In summary, we demonstrated a method for increasing mass transport in CDR: using magnetic fields generated by permanent magnets and orthogonal to the ionic currents generated in the electrochemical cell (i.e., using the Lorentz force). Specifically, we observed that convective fluidic currents generated via the Lorentz force acting on ions enhanced the mass transport in the bulk solution and near the surface of the electrode. Through a combination of (1) PIV, (2) Raman microscopy, and (3) analysis of the limiting-current density, we demonstrate how magnetic fields affect CDR by increasing mass transport and selectivity of CDR over HER. PIV measurements showed that the magnetic fields increase the vorticity (and convection) near the surface of the electrode, and the Raman microscopy measurements showed that this convection decreased the pH gradient near the surface of the electrode. Finally, our analysis of the limiting-current density showed that this increased convection increased the current density (analogous to stirring), and this enhancement in current decreased in magnitude as we increased the viscosity of the solution (for solutions of PEG). Specifically, we observed that an increase in mass transport near the

electrode surface leads to increased current densities (up to 1.3 times higher than the analogous system with no convection) and increased CDR selectivity relative to hydrogen gas production (up to 2.5 times higher than the system with no convection and 1.5 times higher than a model system mechanically mixed with a motor). We excluded (1) effects of gradients in concentration of paramagnetic species and (2) the field-gradient force by performing experiments where we changed the gradient of the B-field while maintaining the same magnitude and direction of the B-field (Figures S21 and S22). When we analyzed the effects of magnetic fields on flow cells with a GDE, the use of a permanent magnet has the potential to reduce the energy consumption of a CO_2 electrolyzer by up to 15% in this case. Convection generated by magnetic fields is compatible with existing methods for increasing mass transport for CDR (GDEs and mechanical agitation) and could help solve the long-standing issues regarding mass transport and concentration polarization for CO_2 electrolyzers.[28–31]

We also identified two future directions for research exploring the intersection of the Lorentz force and CDR: (1) mechanistic exploration of how the Lorentz force interacts with electrochemical systems that produce bubbles (i.e., gas-liquid interfaces) and (2) exploration of how to implement Lorentz force-based mixing in electrolyzers with GDEs to prevent concentration polarization during CDR. We believe a combination of careful experimentation coupled with finite-element simulations can further our understanding of how the Lorentz force affects mass transport in CDR and how electrochemical cells can be designed to maximize these effects.

EXPERIMENTAL PROCEDURES

Resource availability

Lead contact

Future information and requests for resources should be directed to and will be fulfilled by the lead contact, George M. Whitesides (gwhitesides@gmwgroup.harvard.edu).

Materials availability

This study did not generate new reagents.

Data and code availability

Data generated by this work are available upon reasonable request.

Electrochemical cell

We primarily used Cu foil as the cathode and platinum wire as the anode. The Cu foil and Pt wire had >99.9% purity and were obtained from Sigma-Aldrich. Samples were prepared and sealed with rubber septa. Samples were sparged with CO_2 (bone-dry; Airgas) for CDR and Ar (ultra-high purity; Airgas) for reduction of MV for 20 min prior to use. The Cu foils are plasma treated with an air-based plasma in a Harrick plasma chamber at high power (18 W) for varying periods of time.

Electrochemical measurements

Electrochemistry experiments were performed using a CH Instruments electrochemical workstation. An Ag/AgCl (1 M KCl) electrode and a Pt wire were used as the reference and counterelectrodes, respectively, in all measurements. We used a Pt wire rather than a Pt mesh because of the fragility of the Pt mesh, but we did not observe any differences between the two (<1% change in the current; Figure S11). Milli-Q water (18.2 MΩ cm at 25°C) was used in the preparation of all aqueous solutions. CDR experiments were performed on aqueous solutions of 1 M $KHCO_3$ (which served as a buffer, source of CO_2, and electrolyte) and 0.1 M KCl (which served as

additional electrolyte) unless otherwise noted. All of the potentials were calibrated to a RHE. The electrodes were cleaned and polished using 0.05 μm alumina slurry prior to use. All materials were analytical grade (>99%; Millipore-Sigma) and were used as supplied unless otherwise specified.

GC analysis

We performed headspace chromatography (GC) experiments using an Agilent 7890A GC equipped with a ShinCarbon ST packed column (Restek) and a thermal conductivity detector (TCD) with He carrier gas (Figures S17 and S18). To measure the amount of gas formed during bulk electrolysis experiments, we manually injected 100 μL of the sample headspace. The concentration of each species was determined by integrating the area under their respective peak in the chromatogram and comparing with a calibration curve for each species.

Raman microscopy

Raman measurements were carried out using a Horiba LabRam HR Evolution confocal Raman microscope with 532 nm excitation (10 mW). The Raman measurements were averaged over a 1 × 1 μm lateral area using galvo mirrors, and two measurements were collected for 5 s each with a 200-μm pinhole and 600 gr/mm grating. The spectra were corrected for stray cosmic rays, and spectrograph was calibrated to a Si wafer (peak at 520.7 cm^{-1}) prior to each measurement. Analysis and fitting of the Raman spectra were carried out using a procedure described in the supplemental information (Figures S7 and S8).

Measurements of viscosity

We performed measurements of viscosity using a calibrated Brookfield Rotational Viscometer (model DV-III) equipped with a YULA-15 spindle. Before each experiment, the spindle and the sample cup were rinsed with deionized water and dried with a stream of nitrogen gas. The sample cup was loaded with 16 mL of aqueous PEG solutions with a fixed concentration of 0.0556 g/mL and varied molecular weights (400, 1,000, 2,000, 4,000, 6,000, 20,000, 35,000 g/mol), containing 0.1 M $KHCO_3$ + 1M KCl, and was fastened to the instrument, such that the spindle was completely immersed in the liquid. After allowing ~1 min for thermal equilibration, the temperature was measured with a thermocouple and determined to be in the range of 22°C–23°C. A fixed rotational speed of 250 rpm (the maximum speed for the instrument) was employed for all measurements such that the torque on the motor ranged from 19% to 9% of the maximum value, depending on the viscosity of the solution. We note that the minimum torque required for an accurate measurement is reported by the manufacturer to be 10%. Thus, the lower-molecular-weight samples (400, 1,000, 2,000 g/mol) were at the sensitivity limit of the instrument; however, the measured values fit the expected trend, and we believe them to be reasonable.

SUPPLEMENTAL INFORMATION

Supplemental information can be found online at https://doi.org/10.1016/j.checat.2022.01.023.

ACKNOWLEDGMENTS

M.S.K. and R.G. acknowledge the Simons Foundation (award 290364FY21) for partial salary support. S.E.R. acknowledges partial salary support from NSF award CHE-1808361. Sample preparation and characterization were performed in part at the Center for Nanoscale Systems (CNS) at Harvard University, a member of the National Nanotechnology Infrastructure Network (NNIN), which was supported by the

National Science Foundation (ECS0335765). We would like to thank Prof. Jeffrey Bell, Prof. Katja Scorb, and Dr. Haihui Joy Jiang for unpublished experiments that helped inform this work. We would also like to thank Dr. Arthur McClelland for assistance with the Raman microscope and Ed Macomber for assistance with fabricating the gold samples. We would also like to thank Prof. Dan Nocera and Dr. Agnes Thorarinsdottir for lending us a flow cell for the GDE experiments.

AUTHOR CONTRIBUTIONS

M.S.K., R.G., and G.M.W. conceived of the project. M.S.K., R.G., and S.E.R. performed the experiments. All authors wrote the paper.

DECLARATION OF INTERESTS

The authors declare no competing interests.

Received: October 26, 2021
Revised: December 17, 2021
Accepted: January 25, 2022
Published: February 15, 2022

REFERENCES

1. Garza, A.J., Bell, A.T., and Head-Gordon, M. (2018). Mechanism of CO_2 reduction at copper surfaces: pathways to C_2 products. ACS Catal. *8*, 1490–1499. https://doi.org/10.1021/acscatal.7b03477.

2. Cheng, M.-J., Clark, E.L., Pham, H.H., Bell, A.T., and Head-Gordon, M. (2016). Quantum mechanical screening of single-atom bimetallic alloys for the selective reduction of CO_2 to C_1 hydrocarbons. ACS Catal. *6*, 7769–7777. https://doi.org/10.1021/acscatal.6b01393.

3. Bushuyev, O.S., De Luna, P., Dinh, C.T., Tao, L., Saur, G., van de Lagemaat, J., Kelley, S.O., and Sargent, E.H. (2018). What should we make with CO_2 and how can we make it? Joule *2*, 825–832. https://doi.org/10.1016/j.joule.2017.09.003.

4. Feng, X., Jiang, K., Fan, S., and Kanan, M.W. (2015). Grain-Boundary-dependent CO_2 electroreduction activity. J. Am. Chem. Soc. *137*, 4606–4609. https://doi.org/10.1021/ja5130513.

5. Mariano, R.G., McKelvey, K., White, H.S., and Kanan, M.W. (2017). Selective increase in CO_2 electroreduction activity at grain-boundary surface terminations. Science *358*, 1187. https://doi.org/10.1126/science.aao3691.

6. Verdaguer-Casadevall, A., Li, C.W., Johansson, T.P., Scott, S.B., McKeown, J.T., Kumar, M., Stephens, I.E.L., Kanan, M.W., and Chorkendorff, I. (2015). Probing the active surface sites for CO reduction on oxide-derived copper electrocatalysts. J. Am. Chem. Soc. *137*, 9808–9811. https://doi.org/10.1021/jacs.5b06227.

7. Liu, C., Colón, B.C., Ziesack, M., Silver, P.A., and Nocera, D.G. (2016). Water splitting–biosynthetic system with CO_2 reduction efficiencies exceeding photosynthesis. Science *352*, 1210. https://doi.org/10.1126/science.aaf5039.

8. Margarit, C.G., Asimow, N.G., Gonzalez, M.I., and Nocera, D.G. (2020). Double hangman iron porphyrin and the effect of electrostatic nonbonding interactions on carbon dioxide reduction. J. Phys. Chem. Lett. *11*, 1890–1895. https://doi.org/10.1021/acs.jpclett.9b03897.

9. Margarit, C.G., Asimow, N.G., Costentin, C., and Nocera, D.G. (2020). Tertiary amine-assisted electroreduction of carbon dioxide to formate catalyzed by iron tetraphenylporphyrin. ACS Energy Lett. *5*, 72–78. https://doi.org/10.1021/acsenergylett.9b02093.

10. Dogutan, D.K., and Nocera, D.G. (2019). Artificial photosynthesis at efficiencies greatly exceeding that of natural photosynthesis. Acc. Chem. Res. *52*, 3143–3148. https://doi.org/10.1021/acs.accounts.9b00380.

11. Zhang, B.A., Ozel, T., Elias, J.S., Costentin, C., and Nocera, D.G. (2019). Interplay of homogeneous reactions, mass transport, and kinetics in determining selectivity of the reduction of CO_2 on gold electrodes. ACS Cent. Sci. *5*, 1097–1105. https://doi.org/10.1021/acscentsci.9b00302.

12. Verma, S., Kim, B., Jhong, H.-R.M., Ma, S., and Kenis, P.J.A. (2016). A gross-margin model for defining technoeconomic benchmarks in the electroreduction of CO_2. ChemSusChem *9*, 1972–1979. https://doi.org/10.1002/cssc.201600394.

13. Chen, C., Khosrowabadi Kotyk, J.F., and Sheehan, S.W. (2018). Progress toward commercial application of electrochemical carbon dioxide reduction. Chem *4*, 2571–2586. https://doi.org/10.1016/j.chempr.2018.08.019.

14. Voiry, D., Chhowalla, M., Gogotsi, Y., Kotov, N.A., Li, Y., Penner, R.M., Schaak, R.E., and Weiss, P.S. (2018). Best practices for reporting electrocatalytic performance of nanomaterials. ACS Nano *12*, 9635–9638. https://doi.org/10.1021/acsnano.8b07700.

15. Kibria, M.G., Edwards, J.P., Gabardo, C.M., Dinh, C.-T., Seifitokaldani, A., Sinton, D., and Sargent, E.H. (2019). Electrochemical CO_2 reduction into chemical feedstocks: from mechanistic electrocatalysis models to system design. Adv. Mater. *31*, 1807166. https://doi.org/10.1002/adma.201807166.

16. Costentin, C., Robert, M., and Savéant, J.-M. (2015). Current issues in molecular catalysis illustrated by iron porphyrins as catalysts of the CO_2-to-CO electrochemical conversion. Acc. Chem. Res. *48*, 2996–3006. https://doi.org/10.1021/acs.accounts.5b00262.

17. Li, F., Thevenon, A., Rosas-Hernández, A., Wang, Z., Li, Y., Gabardo, C.M., Ozden, A., Dinh, C.T., Li, J., Wang, Y., et al. (2020). Molecular tuning of CO2-to-ethylene conversion. Nature *577*, 509–513. https://doi.org/10.1038/s41586-019-1782-2.

18. Mariano, R.G., Kang, M., Wahab, O.J., McPherson, I.J., Rabinowitz, J.A., Unwin, P.R., and Kanan, M.W. (2021). Microstructural origin of locally enhanced CO_2 electroreduction activity on gold. Nat. Mater. *20*, 1000–1006. https://doi.org/10.1038/s41563-021-00958-9.

19. Costentin, C., Drouet, S., Robert, M., and Savéant, J.-M. (2012). A local proton source enhances CO_2 electroreduction to CO by a molecular Fe catalyst. Science *338*, 90–94. https://doi.org/10.1126/science.1224581.

20. Lee, G., Li, Y.C., Kim, J.-Y., Peng, T., Nam, D.-H., Sedighian Rasouli, A., Li, F., Luo, M., Ip, A.H., Joo, Y.-C., and Sargent, E.H. (2021). Electrochemical upgrade of CO_2 from amine capture solution. Nat. Energy *6*, 46–53. https://doi.org/10.1038/s41560-020-00735-z.

21. de Arquer, F.P.G., Dinh, C.-T., Ozden, A., Wicks, J., McCallum, C., Kirmani, A.R., Nam, D.-H., Gabardo, C., Seifitokaldani, A., and Wang, X. (2020). CO_2 electrolysis to multicarbon products at activities greater than 1 A cm^{-2}. Science *367*, 661–666.

22. Salvatore, D.A., Gabardo, C.M., Reyes, A., O'Brien, C.P., Holdcroft, S., Pintauro, P., Bahar, B., Hickner, M., Bae, C., Sinton, D., et al. (2021). Designing anion exchange membranes for CO_2 electrolysers. Nat. Energy *6*, 339–348. https://doi.org/10.1038/s41560-020-00761-x.

23. Hashiba, H., Weng, L.-C., Chen, Y., Sato, H.K., Yotsuhashi, S., Xiang, C., and Weber, A.Z. (2018). Effects of electrolyte buffer capacity on surface reactant species and the reaction rate of CO_2 in electrochemical CO_2 reduction. J. Phys. Chem. C *122*, 3719–3726. https://doi.org/10.1021/acs.jpcc.7b11316.

24. Wuttig, A., Yoon, Y., Ryu, J., and Surendranath, Y. (2017). Bicarbonate is not a general acid in Au-catalyzed CO_2 electroreduction. J. Am. Chem. Soc. *139*, 17109–17113. https://doi.org/10.1021/jacs.7b08345.

25. Ho, C., and Sturtevant, J.M. (1963). The kinetics of the hydration of carbon dioxide at 25. J. Biol. Chem. *238*, 3499–3501.

26. Pohorecki, R., and Moniuk, W. (1988). Kinetics of reaction between carbon dioxide and hydroxyl ions in aqueous electrolyte solutions. Chem. Eng. Sci. *43*, 1677–1684. https://doi.org/10.1016/0009-2509(88)85159-5.

27. Goyal, A., Marcandalli, G., Mints, V.A., and Koper, M.T.M. (2020). Competition between CO_2 reduction and hydrogen evolution on a gold electrode under well-defined mass transport conditions. J. Am. Chem. Soc. *142*, 4154–4161. https://doi.org/10.1021/jacs.9b10061.

28. Lu, X., Zhu, C., Wu, Z., Xuan, J., Francisco, J.S., and Wang, H. (2020). In situ observation of the pH gradient near the gas diffusion electrode of CO2 reduction in alkaline electrolyte. J. Am. Chem. Soc. *142*, 15438–15444. https://doi.org/10.1021/jacs.0c06779.

29. De Luna, P., Hahn, C., Higgins, D., Jaffer, S.A., Jaramillo, T.F., and Sargent, E.H. (2019). What would it take for renewably powered electrosynthesis to displace petrochemical processes? Science *364*, eaav3506. https://doi.org/10.1126/science.aav3506.

30. Higgins, D., Hahn, C., Xiang, C., Jaramillo, T.F., and Weber, A.Z. (2019). Gas-diffusion electrodes for carbon dioxide reduction: a new paradigm. ACS Energy Lett. *4*, 317–324. https://doi.org/10.1021/acsenergylett.8b02035.

31. Raciti, D., and Wang, C. (2018). Recent advances in CO2 reduction electrocatalysis on copper. ACS Energy Lett. *3*, 1545–1556. https://doi.org/10.1021/acsenergylett.8b00553.

32. Zhang, Z., Melo, L., Jansonius, R.P., Habibzadeh, F., Grant, E.R., and Berlinguette, C.P. (2020). pH matters when reducing CO_2 in an electrochemical flow cell. ACS Energy Lett. *5*, 3101–3107. https://doi.org/10.1021/acsenergylett.0c01606.

33. Welch, A.J., Fenwick, A.Q., Böhme, A., Chen, H.-Y., Sullivan, I., Li, X., DuChene, J.S., Xiang, C., and Atwater, H.A. (2021). Operando local pH measurement within gas diffusion electrodes performing electrochemical carbon dioxide reduction. J. Phys. Chem. C *125*, 20896–20904. https://doi.org/10.1021/acs.jpcc.1c06265.

34. Aogaki, R., Fueki, K., and Mukaibo, T. (1975). Application of magnetohydrodynamic effect to the analysis of electrochemical reactions 1. MHD flow of an electrolyte solution in an electrode-cell with a short rectangular channel. Denki Kagaku Oyobi Kogyo Butsuri Kagaku *43*, 504–508. https://doi.org/10.5796/kogyobutsurikagaku.43.504.

35. Heinmets, F., and Herschman, A. (1961). Considerations on the effects produced by superimposed electric and magnetic fields in biological systems and electrolytes. Phys. Med. Biol. *5*, 271–288. https://doi.org/10.1088/0031-9155/5/3/304.

36. Ragsdale, S.R., Grant, K.M., and White, H.S. (1998). Electrochemically generated magnetic forces. Enhanced transport of a paramagnetic redox species in large, nonuniform magnetic fields. J. Am. Chem. Soc. *120*, 13461–13468. https://doi.org/10.1021/ja982540q.

37. Lioubashevski, O., Katz, E., and Willner, I. (2004). Magnetic field effects on electrochemical processes:A theoretical hydrodynamic model. J. .Phys .Chem .B *108*, 5778–5784. https://doi.org/10.1021/jp037785q.

38. Aaboubi, O., Chopart, J.P., Douglade, J., Olivier, A., Gabrielli, C., and Tribollet, B. (1990). Magnetic field effects on mass transport. J. Electro. Chem. *137*, 1796–1804. https://doi.org/10.1149/1.2086807.

39. Lemoff, A.V., and Lee, A.P. (2000). An AC magnetohydrodynamic micropump. Sens. Actuators B Chem. *63*, 178–185. https://doi.org/10.1016/S0925-4005(00)00355-5.

40. Naaman, R., Paltiel, Y., and Waldeck, D.H. (2019). Chiral molecules and the electron spin. Nat. Rev. Chem. *3*, 250–260. https://doi.org/10.1038/s41570-019-0087-1.

41. Leventis, N., and Dass, A. (2005). Demonstration of the elusive concentration-gradient paramagnetic force. J. Am. Chem. Soc. *127*, 4988–4989. https://doi.org/10.1021/ja043169b.

42. Pan, H., Jiang, X., Wang, X., Wang, Q., Wang, M., and Shen, Y. (2020). Effective magnetic field regulation of the radical pair spin states in electrocatalytic CO_2 reduction. J. Phys. Chem. Lett. *11*, 48–53. https://doi.org/10.1021/acs.jpclett.9b03146.

43. Lewis, A.M., Fay, T.P., Manolopoulos, D.E., Kerpal, C., Richert, S., and Timmel, C.R. (2018). On the low magnetic field effect in radical pair reactions. J. Chem. Phys. *149*, 034103. https://doi.org/10.1063/1.5038558.

44. Molokov, S.S., Moreau, R., and Moffatt, H.K. (2007). Magnetohydrodynamics: Historical Evolution and Trends (Springer Science & Business Media).

45. Bhargava, S.S., Azmoodeh, D., Chen, X., Cofell, E.R., Esposito, A.M., Verma, S., Gewirth, A.A., and Kenis, P.J.A. (2021). Decreasing the energy consumption of the CO_2 electrolysis process using a magnetic field. ACS Energy Lett. *6*, 2427–2433. https://doi.org/10.1021/acsenergylett.1c01029.

46. Kubo, R. (1966). The fluctuation-dissipation theorem. Rep. Prog. Phys. *29*, 255–284. https://doi.org/10.1088/0034-4885/29/1/306.

47. Feynman, R.P. (2006). The Feynman Lectures on Physics, Definitive ed (Pearson/Addison-Wesley).

48. Feynman, R.P., Leighton, R.B., and Sands, M. (1964). In The Feynman Lectures on Physics, Vol II: The New Millenium Edition: Mainly Electromagnetism and Matter. Mainly Electromagnetism and Matter (Basic Books), pp. 39–1–41–12.

49. Raffel, M., Willert, C.E., Scarano, F., Kähler, C.J., Wereley, S.T., and Kompenhans, J. (2018). Particle Image Velocimetry: A Practical Guide (Springer).

50. Michaelis, L., and Hill, E.S. (1933). The viologen indicators. J. Gen. Physiol. *16*, 859–873.

51. Seh, Z.W. (2017). Combining theory and experiment in electrocatalysis: insights into materials design. Science *355*. https://doi.org/10.1126/science.aad4998.

52. Devos, O., Aaboubi, O., Chopart, J.-P., Olivier, A., Gabrielli, C., and Tribollet, B. (2000). Is there a magnetic field effect on electrochemical kinetics? J. Phys. Chem. A. *104*, 1544–1548. https://doi.org/10.1021/jp993696v.

53. Hinds, G., Spada, F.E., Coey, J.M.D., Ní Mhíocháin, T.R., and Lyons, M.E.G. (2001). Magnetic field effects on copper electrolysis. J. Phys. Chem. B *105*, 9487–9502. https://doi.org/10.1021/jp010581u.

54. Yang, X., Baczyzmalski, D., Cierpka, C., Mutschke, G., and Eckert, K. (2018). Marangoni convection at electrogenerated hydrogen bubbles. Phys. Chem. Chem. Phys. *20*, 11542–11548. https://doi.org/10.1039/C8CP01050A.

55. Zhang, W., Huang, C., Xiao, Q., Yu, L., Shuai, L., An, P., Zhang, J., Qiu, M., Ren, Z., and Yu, Y. (2020). Atypical oxygen-bearing copper boosts ethylene selectivity toward electrocatalytic CO_2 reduction. J. Am. Chem. Soc. *142*, 11417–11427. https://doi.org/10.1021/jacs.0c01562.

56. Jouny, M., Luc, W.W., and Jiao, F. (2018). General techno-economic analysis of CO2 electrolysis systems. Ind. Eng. Chem. Res. *57*. https://doi.org/10.1021/acs.iecr.7b03514.

57. Shin, H., Hansen, K.U., and Jiao, F. (2021). Techno-economic assessment of low-temperature carbon dioxide electrolysis. Nat. Sustain. *4*, 911–919. https://doi.org/10.1038/s41893-021-00739-x.